Publications of the Astronomical Society of the Pacific
107: 1047–1054, 1995 November

Photometric Calibration of Hydrogen- and Helium-Rich White-Dwarf Models

P. BERGERON, F. WESEMAEL, AND A. BEAUCHAMP

Département de Physique, Université de Montréal, C.P. 6128, Succ. Centre-Ville, Montréal, Québec, Canada, H3C 3J7
Electronic mail: bergeron@astro.umontreal.ca, wesemael@astro.umontreal.ca, beaucham@cae.ca

Received 1995 June 28; accepted 1995 August 14

ABSTRACT. Bolometric corrections and color indices on various photometric systems are provided for an extensive grid of hydrogen- and helium-rich white-dwarf model atmospheres. Absolute visual magnitudes, masses, and ages are also obtained for each model from detailed evolutionary cooling sequences appropriate for these stars. The results of our calculations are briefly compared with published observational material. These calculations can easily be extended to any given photometric system.

1. INTRODUCTION

Two-color diagrams, as well as color–magnitude diagrams, can reveal a wealth of information about the nature and physical properties of various stellar populations. The first comprehensive analyses of white-dwarf stars, for instance, were accomplished in this manner. Among the most important studies of the hydrogen-line (DA) white dwarfs, we mention those of Koester et al. (1979), Shipman and Sass (1980), Weidemann and Koester (1984), and Fontaine et al. (1985), who combined either Johnson, Strömgren, or multichannel photometry with theoretical predictions from model-atmosphere calculations to determine the surface gravity (or mass) and temperature distributions of DA stars. Similar studies for DB stars include those of Koester et al. (1981) and Oke et al. (1984).

These photometric studies have now been superseded by spectroscopic analyses which provide more precise atmospheric parameters from a detailed comparison of observed and synthetic line profiles (see, e.g., Bergeron et al. 1992 for the DA stars, and Beauchamp 1995 for the DB stars). This improved understanding of the physical properties of white-dwarf stars combined with evolutionary model calculations (see, e.g., Wood 1992) has lead to the interesting possibility of using white dwarfs in distant clusters to infer fundamental parameters about the clusters themselves, such as their ages or distances (Fusi Pecci and Renzini 1979). Recent observations with the *Hubble Space Telescope* (*HST*) have been aimed specifically at detecting white dwarfs in both open and globular clusters. For instance, von Hippel et al. (1995) have identified the white-dwarf sequence in two open clusters, NGC 2477 and NGC 2420, and demonstrated the feasibility of using the observed low-luminosity cutoff to estimate the age of the clusters. This technique had been first applied successfully to infer the age of the local Galactic disk using nearby white dwarfs (Winget et al. 1987; Wood 1992).

White dwarfs have recently been detected in several globular clusters as well (Paresce et al. 1995; Elson et al. 1995; De Marchi and Paresce 1995; Richer et al. 1995). Most noteworthy are the *HST* photometric observations of the globular cluster M4 by Richer et al. (1995), which reveal a very narrow white-dwarf sequence of about 70 stars. The authors have used the calculations presented in this article to infer a mean mass of $\sim 0.5\ M_{\odot}$ for the observed (mostly hot, $T_{\rm eff} \gtrsim 10{,}000$ K) white dwarfs, in excellent agreement with the theoretical expectations discussed by Fusi Pecci and Renzini (1979).

Despite the higher accuracy of spectroscopic analyses, the spectroscopic technique can only be applied successfully to relatively bright, and thus nearby, white dwarfs. Unfortunately, high signal-to-noise spectroscopy is a luxury one cannot yet afford for studying a large number of white dwarfs in the more distant open or globular clusters. Consequently, one is forced to rely upon broadband photometry to study the white-dwarf population in such distant clusters. There is therefore an immediate need for photometric calibrations of both DA and non-DA white-dwarf models. Koester et al. (1979) have published the most extensive set of color indices for DA stars. Although the physics of DA models above $T_{\rm eff} \sim 15{,}000$ has not changed much since then, that of the cooler stars where convection and molecular hydrogen become important have been revised significantly. Furthermore, new results for both hot and cool pure helium white-dwarf atmospheres have recently become available (see Sec. 2), so that it is now possible to calculate more realistic color indices for these stars as well. Perhaps more importantly, absolute visual magnitudes require the knowledge of precise bolometric corrections, few of which are available in the literature.

To overcome this situation, we thus present the results of a color-index and magnitude calculation for an extensive grid of self-consistent hydrogen- and helium-rich models. In Sec. 2, we briefly describe the model atmospheres which are used in Sec. 3 to calculate color indices on various photometric systems. White-dwarf cooling sequences are also combined with these results to derive the mass, the absolute visual magnitude, and the age of each model. We finally compare our results with photometric and trigonometric parallax data available in the literature. While only a subset of these results is presented here, the complete set of our calculations can be made available upon request.

2. MODEL-ATMOSPHERE CALCULATIONS

Our pure hydrogen models are described at length in Wesemael et al. (1980), Bergeron et al. (1991; see also Bergeron et al. 1992), and Bergeron et al. (1995a,b). These models contain the appropriate physics for the calculation of white-dwarf models in the temperature range of interest ($100{,}000 \geq T_{\rm eff} \geq 4000$ K). Specifically, convective energy

transport is included in models below $T_{\rm eff}$=17,000 K, and treated within the so-called ML2/α=0.6 parameterization of the mixing-length theory (see Bergeron et al. 1995b for details). Furthermore, the collision-induced opacity by molecular hydrogen is included using new results discussed by Bergeron et al. (1995a). For the purpose of this article, particular attention has been paid to calculate all hydrogen lines present in the emergent spectrum, and to treat the merging of the hydrogen lines at each jump within the occupation formalism of Hummer and Mihalas (1988). The color calculations in the near- and far-infrared are particularly sensitive to the inclusion of these additional lines. For instance, Bergeron et al. (1995a) did not include the hydrogen-line opacity at the Paschen jump, but instead described the Paschen jump as a simple photoionization edge. The more detailed treatment used here yields results which are significantly different from some color indices published by Bergeron et al., at least for the hotter models where these lines are important.

Our model atmospheres with pure helium compositions are described in Bergeron et al. (1995a), Beauchamp et al. (1995), Beauchamp (1995). Here, we restrict the calculations to white-dwarf models below the so-called DB gab ($T_{\rm eff}$<30,000 K). In his DB model calculations, Beauchamp (1995) has introduced the continuous absorption opacity of He_2^+ developed by Stancil (1994), an important source of opacity in cool ($T_{\rm eff}\leq$16,000 K), pure helium models which had been neglected in the model grid of Bergeron et al. (1995a; $T_{\rm eff}\leq$10,000 K). To ensure a continuity between both grids, we have recalculated the models of Bergeron et al. (1995a) and included this additional opacity source. Although the He_2^+ opacity is completely negligible below $T_{\rm eff}\sim$6500 K, the difference in the emergent fluxes can reach 5% at V in models around 10,000 K.

Our model grid covers a range in log g of 7.0 (0.5) 9.0, where the number in parentheses indicates the step in log g. In effective temperature, the pure hydrogen grid covers the range $T_{\rm eff}$=4000 (500) 8000 (1000) 17,000, 20,000 (5000) 100,000 K, while the pure helium grid covers the range $T_{\rm eff}$=4000 (250) 5500 (500) 10,000 (1000) 15,000, 17,000, 18,000 (2000) 30,000 K.

In Fig. 1, we show two representative energy distributions of DA and DB models. The wavelength range displayed is much larger than that required here, but it illustrates the possibility of extending the color calculations to any wavelength range.

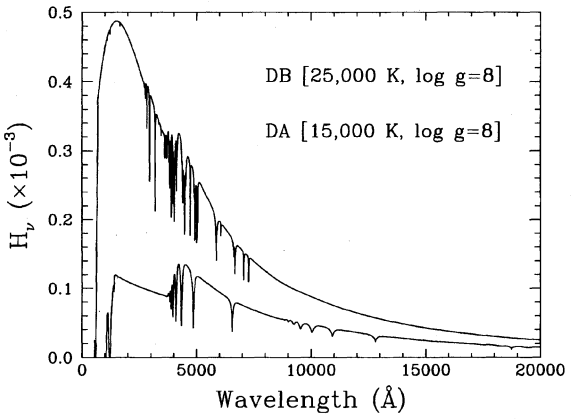

FIG. 1—Eddington fluxes (in ergs cm^{-2} s^{-1} Hz^{-1} str^{-1}) for two illustrative energy distributions used in our color calculations. The atmospheric parameters of the DB (top) and DA (bottom) spectra are indicated on the plot.

3. RESULTS

3.1 Bolometric Correction, Absolute Visual Magnitude, Mass, and Age

For internal consistency with the color calculations presented in the following sections, we first rederive an expression for the bolometric correction similar to that of Wesemael et al. [1980; Eq. (A.10)]. We start from Eq. (A.8) of Wesemael et al. (1980)

$$\mathrm{BC}=2.5\ \log\left[\frac{\int_0^\infty f_\lambda S_V(\lambda)d\lambda}{\int_0^\infty f_\lambda d\lambda}\right]+\mathrm{BC}_\odot$$

$$-2.5\ \log\left[\frac{\int_0^\infty f_\lambda^\odot S_V(\lambda)d\lambda}{\int_0^\infty f_\lambda^\odot d\lambda}\right], \qquad (1)$$

where f_λ is the observed emergent flux distribution, $S_V(\lambda)$ is the transmission function of the V filter, and $\mathrm{BC}_\odot$ is the bolometric correction of the Sun ($\mathrm{BC}_\odot=-0.08$; this value for $\mathrm{BC}_\odot$ and the physical constants used below for the Sun are taken from Allen 1973). The transmission function of the V filter employed by Wesemael et al. (1980) was that of Matthews and Sandage (1963) while we rely in this analysis on that of Bessell (1990). The second term in brackets can be evaluated by using the integrated solar flux outside Earth's atmosphere, $f^\odot\equiv\int_0^\infty f_\lambda^\odot d\lambda=1.360\times10^6$ erg s^{-1} cm^{-2}, the observed visual magnitude of the Sun ($V_\odot=-26.74$), and the relation connecting the visual magnitude to the observed flux at Earth

$$V=-2.5\ \log\left[\frac{\int_0^\infty f_\lambda S_V(\lambda)d\lambda}{\int_0^\infty S_V(\lambda)d\lambda}\right]-21.1158, \qquad (2)$$

where the constant has been derived using the Vega flux described in Sec. 3.2. We finally obtain the expression

$$\mathrm{BC}=2.5\ \log\int_0^\infty H_\lambda S_V(\lambda)d\lambda-10\ \log T_{\rm eff}+15.6165, \qquad (3)$$

where H_λ is the monochromatic Eddington flux from the model atmosphere at temperature $T_{\rm eff}$ (in Wesemael et al. 1980, the constant of Eq. [3] assumed the value 14.311 since the transmission function of Matthews and Sandage 1963 was used). We note that the expression for the bolometric correction is independent of any mass-radius relationship.

The bolometric magnitude $M_{\rm bol}$ (or the absolute visual magnitude, $M_V=M_{\rm bol}-\mathrm{BC}$), however, requires such a relation between the mass and the radius of the star since

$$M_{\rm bol}=-2.5\ \log L/L_\odot+M_{\rm bol}^\odot, \qquad (4)$$

where $L_\odot$ and $M_{\rm bol}^\odot$ are the luminosity and the bolometric magnitude of the Sun, respectively ($L_\odot=3.826\times10^{33}$ erg s^{-1}, $M_{\rm bol}^\odot=+4.75$), and $L=4\pi R^2\sigma T_{\rm eff}^4$ is the luminosity

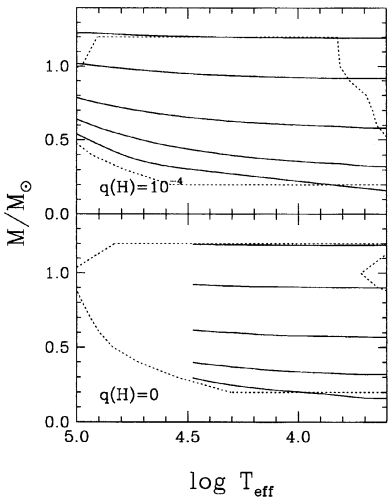

FIG. 2—Location of constant log g values in the mass–$T_{\rm eff}$ plane, interpolated (or extrapolated) from the evolutionary models of Wood (1990,1995). In each panel, the solid lines indicate models with log g=7.0, 7.5, 8.0, 8.5, and 9.0 (from bottom to top). Cooling sequences with thick hydrogen layers [q(H)=10^{-4}] are used for the pure hydrogen-model grid (top panel), while sequences with no hydrogen layer [q(H)=0] are used for the pure helium-model grid (bottom panel). The dashed lines delineate the areas covered by Wood's models, outside of which the stellar masses are extrapolated.

of the star, and R is the corresponding radius which must be evaluated from evolutionary models.

An alternative expression for the bolometric correction can be derived by substituting in Eq. (2) for V the observed flux at Earth by its value at the stellar surface, $f_\lambda = 4\pi(R/D)^2 H_\lambda$, where D is the distance from Earth. Then one obtains an expression for M_V by setting D=10 pc, which can be subtracted from $M_{\rm bol}$ to obtain BC. The constant in Eq. (3) then becomes 15.6146, in excellent agreement with the value of 15.6165 derived above.

We rely on two different sets of evolutionary models for the hydrogen- and helium-rich models. For the latter, we use the cooling sequences of Wood (1990) for carbon-core compositions, helium layers of $q(\mathrm{He}) \equiv M_{\rm He}/M_\star = 10^{-4}$, and no hydrogen layers. For the hydrogen-rich models, we use the more recent evolutionary models of Wood (1995) for carbon-core compositions, helium layers of q(He)=10^{-2}, and thick hydrogen layers of q(H)=10^{-4}. Both grids of evolutionary models cover a range in mass of 0.4−1.2 $M_\odot$; for lower masses, we use unpublished 0.2 and 0.3 $M_\odot$ models kindly provided by Wood for the purpose of our analysis. Since the models of Wood (1990,1995) do not cover completely the $T_{\rm eff}$−log g plane of our model-atmosphere grid, we use a smooth extrapolation outside this range. For the log g=7.0 models at low temperatures, we further impose that the extrapolated masses be always larger than the limit of Hamada and Salpeter (1961), $M \geqslant 0.16 M_\odot$. The DA and non-DA models at constant log g are shown in the $T_{\rm eff}$−M plane in Fig. 2, together with the regions covered by the models of Wood (1990,1995).

Tables 1 and 2 summarize our results for the log g=8.0 model atmospheres with pure hydrogen and pure helium compositions, respectively, where the mass, the bolometric correction, the absolute visual magnitude, the age, and the average V flux (see Sec. 3.6) are given for each model. The masses can be used, in particular, to calculate color sequences for a constant *mass* value (instead of constant log g).

TABLE 1
Calibration for the Pure Hydrogen log g=8 Models

$T_{\rm eff}$(K)	$M/M_\odot$	BC(V)	M_V	Age (yrs)	H_V^a
4000	0.580	−0.267	16.105	8.47×10^9	1.27×10^5
4500	0.581	−0.299	15.625	7.02×10^9	1.98×10^5
5000	0.582	−0.246	15.111	5.39×10^9	3.16×10^5
5500	0.585	−0.177	14.623	3.57×10^9	4.93×10^5
6000	0.589	−0.131	14.192	2.32×10^9	7.29×10^5
6500	0.592	−0.131	13.840	1.91×10^9	1.00×10^6
7000	0.594	−0.152	13.535	1.60×10^9	1.32×10^6
7500	0.595	−0.178	13.259	1.34×10^9	1.70×10^6
8000	0.597	−0.212	13.010	1.14×10^9	2.13×10^6
9000	0.600	−0.268	12.549	8.43×10^8	3.25×10^6
10000	0.603	−0.330	12.148	6.46×10^8	4.67×10^6
11000	0.605	−0.441	11.841	5.09×10^8	6.18×10^6
12000	0.607	−0.611	11.629	4.09×10^8	7.48×10^6
13000	0.610	−0.828	11.494	3.32×10^8	8.44×10^6
14000	0.612	−1.018	11.358	2.71×10^8	9.53×10^6
15000	0.614	−1.198	11.234	2.23×10^8	1.06×10^7
16000	0.617	−1.370	11.121	1.84×10^8	1.18×10^7
17000	0.619	−1.529	11.013	1.52×10^8	1.29×10^7
20000	0.627	−1.967	10.732	8.53×10^7	1.66×10^7
25000	0.639	−2.546	10.321	2.98×10^7	2.37×10^7
30000	0.650	−2.966	9.931	1.17×10^7	3.34×10^7
35000	0.661	−3.343	9.620	6.33×10^6	4.38×10^7
40000	0.672	−3.742	9.421	4.02×10^6	5.17×10^7
45000	0.682	−4.121	9.272	2.81×10^6	5.84×10^7
50000	0.694	−4.473	9.149	1.82×10^6	6.44×10^7
55000	0.703	−4.799	9.046	1.53×10^6	6.99×10^7
60000	0.713	−5.099	8.953	1.26×10^6	7.50×10^7
65000	0.722	−5.376	8.868	1.05×10^6	8.00×10^7
70000	0.732	−5.634	8.791	9.01×10^5	8.49×10^7
75000	0.741	−5.875	8.719	7.77×10^5	8.96×10^7
80000	0.750	−6.101	8.651	6.76×10^5	9.43×10^7
85000	0.759	−6.312	8.586	5.91×10^5	9.89×10^7
90000	0.768	−6.511	8.524	5.20×10^5	1.03×10^8
95000	0.777	−6.699	8.464	4.57×10^5	1.08×10^8
100000	0.785	−6.878	8.408	4.02×10^5	1.12×10^8

[a]units of ergs cm^{-2} s^{-1} $\mathrm{\AA}^{-1}$ str^{-1}.

3.2 Calibration Using the Vega Fluxes

A color index, say $B-V$, is obtained from the equation

$$B-V = -2.5 \log\left[\frac{\int_0^\infty H_\lambda S_B(\lambda)\,d\lambda}{\int_0^\infty H_\lambda S_V(\lambda)\,d\lambda}\right] + C_{B-V}, \qquad (5)$$

where C_{B-V} is a constant which remains to be evaluated. In the following, we use Vega as the flux standard and *assume* that each magnitude and color index are identical to zero. Then the constant in Eq. (5) can be evaluated in a straightforward manner. Here we reconstruct the Vega fluxes from three different studies. In the optical, we use the observed fluxes of Vega measured by Hayes (1985), while in the infrared we use the results of Mountain et al. (1985). These data sets are displayed in Fig. 3 together with the Strömgren *ubvy*, the Johnson–Cousins *UBVRI*, and the Johnson–Glass *JHK* response functions. Also displayed are the model fluxes from Castelli and Kurucz (1994) at $T_{\rm eff}$=9550 K, log g =3.95, normalized at 5000 Å. Since the model fluxes give a better representation of the high Balmer lines and also of the flux shortward of 3300 Å, we use these in our calculations for λ<4500 Å. We also find that the model fluxes are under-

TABLE 2
Calibration for the Pure Helium log g=8 Models

$T_{\rm eff}$(K)	$M/M_\odot$	BC(V)	M_V	Age (yrs)	H_V^a
4000	0.569	−0.963	16.822	9.97×10^9	6.69×10^4
4250	0.570	−0.697	16.292	8.93×10^9	1.09×10^5
4500	0.570	−0.487	15.834	7.85×10^9	1.66×10^5
4750	0.570	−0.327	15.439	6.71×10^9	2.39×10^5
5000	0.570	−0.209	15.098	5.62×10^9	3.27×10^5
5250	0.571	−0.127	14.801	4.72×10^9	4.29×10^5
5500	0.572	−0.073	14.544	3.99×10^9	5.43×10^5
6000	0.573	−0.025	14.116	3.00×10^9	8.04×10^5
6500	0.574	−0.024	13.766	2.49×10^9	1.11×10^6
7000	0.575	−0.046	13.465	2.10×10^9	1.46×10^6
7500	0.575	−0.085	13.203	1.76×10^9	1.86×10^6
8000	0.575	−0.135	12.973	1.49×10^9	2.29×10^6
8500	0.575	−0.196	12.770	1.28×10^9	2.77×10^6
9000	0.577	−0.264	12.587	1.11×10^9	3.26×10^6
9500	0.578	−0.338	12.424	9.63×10^8	3.79×10^6
10000	0.579	−0.416	12.278	8.44×10^8	4.33×10^6
11000	0.579	−0.570	12.017	6.53×10^8	5.49×10^6
12000	0.581	−0.732	11.798	5.12×10^8	6.69×10^6
13000	0.584	−0.892	11.605	4.04×10^8	7.95×10^6
14000	0.585	−1.044	11.432	3.21×10^8	9.29×10^6
15000	0.587	−1.186	11.271	2.56×10^8	1.07×10^7
17000	0.593	−1.442	10.973	1.64×10^8	1.40×10^7
18000	0.595	−1.567	10.845	1.32×10^8	1.57×10^7
20000	0.599	−1.829	10.643	8.52×10^7	1.88×10^7
22000	0.601	−2.119	10.514	5.44×10^7	2.10×10^7
24000	0.605	−2.444	10.455	3.62×10^7	2.21×10^7
26000	0.609	−2.722	10.378	2.57×10^7	2.35×10^7
28000	0.613	−2.946	10.274	1.94×10^7	2.58×10^7
30000	0.616	−3.143	10.165	1.54×10^7	2.83×10^7

[a]units of ergs cm^{-2} s^{-1} Å^{-1} str^{-1}.

TABLE 3
Broadband Color Indices for the Pure Hydrogen log g= 8 Models

$T_{\rm eff}$(K)	$U-B$	$B-V$	$V-I$	$R-I$	$V-K^a$	$J-H^a$	$H-K^a$
4000	+0.182	+0.976	+1.249	+0.620	+1.309	−0.152	−0.126
4500	+0.050	+0.866	+1.126	+0.564	+1.756	+0.085	−0.019
5000	−0.081	+0.752	+0.980	+0.491	+1.828	+0.243	+0.056
5500	−0.200	+0.646	+0.844	+0.422	+1.650	+0.260	+0.082
6000	−0.326	+0.538	+0.716	+0.358	+1.390	+0.236	+0.056
6500	−0.434	+0.445	+0.605	+0.303	+1.161	+0.212	+0.028
7000	−0.510	+0.374	+0.515	+0.258	+0.959	+0.185	+0.007
7500	−0.559	+0.321	+0.437	+0.219	+0.775	+0.156	−0.009
8000	−0.592	+0.283	+0.366	+0.188	+0.607	+0.129	−0.023
9000	−0.603	+0.236	+0.241	+0.123	+0.300	+0.078	−0.045
10000	−0.587	+0.215	+0.125	+0.065	+0.033	+0.036	−0.060
11000	−0.580	+0.197	+0.028	+0.016	−0.169	+0.006	−0.069
12000	−0.591	+0.177	−0.042	−0.019	−0.302	−0.011	−0.074
13000	−0.605	+0.153	−0.086	−0.041	−0.376	−0.021	−0.073
14000	−0.636	+0.119	−0.121	−0.060	−0.444	−0.031	−0.076
15000	−0.677	+0.083	−0.144	−0.074	−0.499	−0.039	−0.079
16000	−0.720	+0.050	−0.163	−0.086	−0.546	−0.047	−0.083
17000	−0.763	+0.020	−0.179	−0.096	−0.588	−0.053	−0.086
20000	−0.873	−0.044	−0.216	−0.119	−0.705	−0.063	−0.106
25000	−1.008	−0.125	−0.265	−0.149	−0.845	−0.083	−0.122
30000	−1.109	−0.191	−0.301	−0.172	−0.953	−0.099	−0.135
35000	−1.169	−0.235	−0.315	−0.182	−0.995	−0.109	−0.135
40000	−1.198	−0.258	−0.324	−0.188	−1.015	−0.114	−0.133
45000	−1.215	−0.273	−0.330	−0.192	−1.028	−0.117	−0.132
50000	−1.227	−0.284	−0.334	−0.195	−1.038	−0.120	−0.132
55000	−1.236	−0.292	−0.339	−0.198	−1.046	−0.122	−0.132
60000	−1.243	−0.299	−0.341	−0.199	−1.053	−0.123	−0.132
65000	−1.249	−0.304	−0.344	−0.201	−1.059	−0.125	−0.132
70000	−1.254	−0.309	−0.347	−0.203	−1.065	−0.126	−0.132
75000	−1.259	−0.313	−0.349	−0.204	−1.071	−0.127	−0.132
80000	−1.263	−0.317	−0.350	−0.205	−1.076	−0.128	−0.133
85000	−1.266	−0.321	−0.353	−0.207	−1.080	−0.129	−0.133
90000	−1.269	−0.324	−0.355	−0.208	−1.085	−0.130	−0.133
95000	−1.272	−0.326	−0.356	−0.209	−1.089	−0.131	−0.134
100000	−1.275	−0.329	−0.358	−0.210	−1.093	−0.131	−0.134

[a]All infrared photometric indices are on the CIT system.

estimated in the near- and far-infrared, and we thus prefer to rely on the observed fluxes of Mountain et al. (1985); a smooth interpolation in (λ, $\log f_\lambda$) is used for $\lambda>1.05$ μm (also shown in Fig. 3). In the next subsections, we discuss the details of the color-index calculations, and present a brief comparison with observational material.

3.3 Johnson Photometry

Broadband photometry is calculated using the Johnson–Cousins *UBVRI* transmission functions from Bessel (1990),

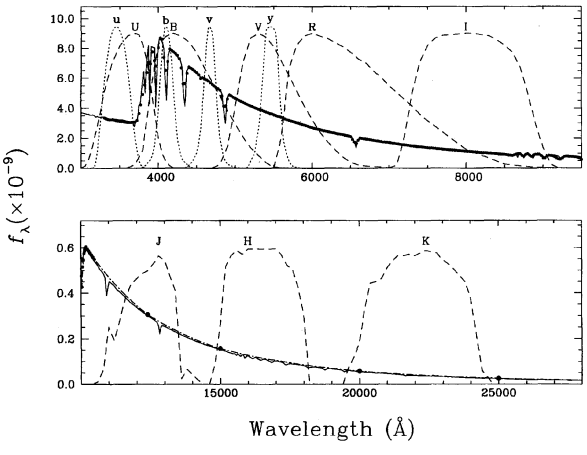

FIG. 3—Observed energy distribution of Vega (in ergs cm^{-2} s^{-1} Å^{-1}). The dots represent the data from Hayes (1985) in the optical and that of Mountain et al. (1985) in the infrared. The solid line indicates the model fluxes from Castelli and Kurucz (1994) normalized at 5000 Å, while the dash–dotted line represents our interpolation of the flux in the infrared using the data of Mountain et al. Also displayed are the filter transmissions of the *ubvy* Strömgren, *UBVRI* Johnson–Cousins, and *JHK* Johnson–Glass systems.

and those of the Johnson–Glass *JHK* system from Bessel and Brett (1988). The infrared color indices are converted from the Johnson–Glass system to the CIT system using the following equations

$$(V-K)_{\rm CIT}=0.999(V-K)_{\rm JG}+0.02, \quad (6)$$

$$(J-H)_{\rm CIT}=0.911(J-H)_{\rm JG}+0.002, \quad (7)$$

$$(H-K)_{\rm CIT}=0.970(H-K)_{\rm JG}, \quad (8)$$

determined by Leggett (1992). Our results are summarized in Tables 3 and 4 for the log g=8.0 pure hydrogen and pure helium models, respectively.

In Fig. 4, we show the [$(U-B)$,$(B-V)$] two-color diagrams for the DA and non-DA models. The observed photometry and trigonometric parallax data used here and below are taken from the new Yale parallax catalog (van Altena et al. 1994), and divided into DA and non-DA stars. The results of Fig. 4 for the DA stars are practically identical to those displayed in Fig. 1 of Koester et al. (1979), with all stars falling on a line of almost constant surface gravity with very little dispersion. There is also a small indication in this plot that DA stars have a mean log g value slightly below 8.0, a result which has been confirmed by the detailed spectroscopic analysis of Bergeron et al. (1992) who determined $\langle\log g\rangle$=7.91 for a sample of 129 DA stars hotter than $T_{\rm eff}\sim$13,000 K.

In contrast, the non-DA stars reveal a much more important scatter in the $(U-B)$ direction which cannot be accounted for by a simple spread in log g. Indeed, theoretical models predict that all white-dwarf stars with pure helium compositions below $T_{\rm eff}\sim$13,000 K should lie on a single sequence. The obvious reason for the observed spread is the

TABLE 4
Broadband Color Indices for the Pure Helium log g=8 Models

$T_{\rm eff}$(K)	$U-B$	$B-V$	$V-I$	$R-I$	$V-K^a$	$J-H^a$	$H-K^a$
4000	+0.988	+1.561	+1.780	+0.848	+3.200	+0.330	+0.216
4250	+0.804	+1.396	+1.560	+0.744	+2.784	+0.291	+0.189
4500	+0.625	+1.239	+1.366	+0.653	+2.427	+0.258	+0.167
4750	+0.453	+1.092	+1.200	+0.575	+2.123	+0.230	+0.148
5000	+0.291	+0.959	+1.058	+0.508	+1.865	+0.206	+0.131
5250	+0.141	+0.841	+0.939	+0.452	+1.646	+0.186	+0.116
5500	+0.007	+0.740	+0.840	+0.405	+1.461	+0.167	+0.103
6000	−0.204	+0.583	+0.686	+0.331	+1.164	+0.136	+0.080
6500	−0.347	+0.476	+0.577	+0.277	+0.935	+0.110	+0.059
7000	−0.446	+0.398	+0.491	+0.233	+0.747	+0.086	+0.041
7500	−0.524	+0.334	+0.417	+0.195	+0.585	+0.066	+0.025
8000	−0.589	+0.279	+0.354	+0.163	+0.445	+0.048	+0.010
8500	−0.645	+0.230	+0.298	+0.134	+0.321	+0.033	−0.002
9000	−0.694	+0.187	+0.249	+0.108	+0.213	+0.019	−0.013
9500	−0.737	+0.150	+0.206	+0.086	+0.116	+0.007	−0.023
10000	−0.775	+0.116	+0.168	+0.066	+0.031	−0.004	−0.031
11000	−0.836	+0.064	+0.106	+0.035	−0.108	−0.022	−0.045
12000	−0.885	+0.021	+0.053	+0.009	−0.226	−0.037	−0.057
13000	−0.924	−0.012	+0.011	−0.012	−0.324	−0.050	−0.066
14000	−0.953	−0.037	−0.027	−0.031	−0.408	−0.061	−0.074
15000	−0.973	−0.055	−0.060	−0.047	−0.480	−0.071	−0.081
17000	−0.995	−0.072	−0.112	−0.069	−0.592	−0.088	−0.092
18000	−1.002	−0.077	−0.134	−0.078	−0.631	−0.094	−0.095
20000	−1.016	−0.088	−0.169	−0.092	−0.688	−0.103	−0.097
22000	−1.028	−0.102	−0.193	−0.103	−0.725	−0.108	−0.098
24000	−1.034	−0.110	−0.204	−0.109	−0.739	−0.109	−0.097
26000	−1.043	−0.123	−0.216	−0.116	−0.756	−0.109	−0.096
28000	−1.058	−0.142	−0.234	−0.126	−0.787	−0.111	−0.097
30000	−1.077	−0.161	−0.249	−0.136	−0.820	−0.114	−0.100

[a]All infrared photometric indices are on the CIT system.

presence of a wide variety of objects in the non-DA spectral class, such as DQ and DZ stars, with strong absorption features in the optical which are not taken into account in our calculations. The overall location of non-DA stars in Fig. 4 is nonetheless well reproduced by our pure helium models.

Figure 5 displays the $[M_V,(B-V)]$ diagrams for the same data set. Here the change in radius as a function of log g is reflected by a vertical shift in M_V. Again, the hotter white dwarfs are characterized by a mean surface gravity slightly below 8.0, but there also seems to be a trend for the coolest white dwarfs to have larger masses. Since these cool remnants were presumably formed from more massive progenitors, it is perhaps not surprising that their masses be larger than the average mass of hotter white dwarfs. There are also several DA stars with inferred surface gravities smaller than log g=7.0. However, a closer inspection of these objects reveals that they are either composites, or their trigonometric parallax is uncertain. Surprisingly, the observed non-DA sequence is very narrow this time, with a clear indication of a larger mean surface gravity than the DA stars, except perhaps at the cool end of the cooling sequence. The two stars above the log g=7.0 sequence correspond to the DQ6 star L 845−70 ($B-V=+0.02$) with an uncertain trigonometric parallax measurement of π=0.0032±0.0182 arcsec, and to G 147−65 ($B-V=+1.05$), a white dwarf +M-dwarf system, with combined colors most likely contaminated by the M-dwarf component.

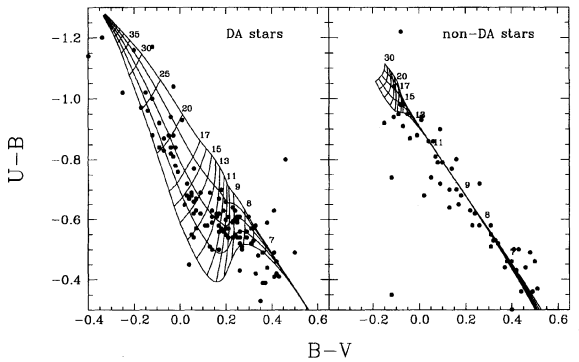

FIG. 4—[$(U-B),(B-V)$] two-color diagrams for the DA and non-DA models with $T_{\rm eff}$ indicated in units of 10^3 K, and log g values of 7.0 (0.5) 9.0 (from bottom to top). The observed photometry is taken from the new Yale parallax catalog of van Altena et al. (1994).

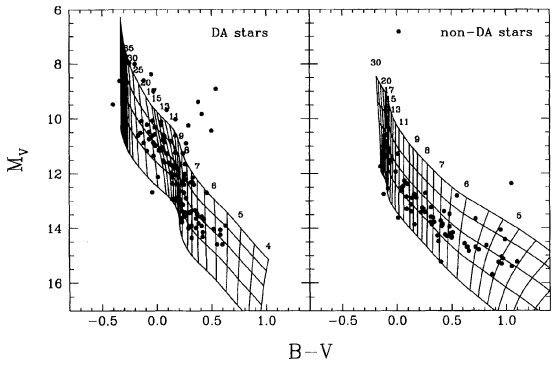

FIG. 5—Same as Fig. 4 but for the $[M_V,(B-V)]$ diagrams, with the exception that the values of log g are for 7.0 (0.5) 9.0 from top to bottom.

Another sample of interest is provided by the USNO trigonometric parallax program (Monet et al. 1992, and references therein). The white-dwarf component of the USNO data set is plotted in the $[M_V,(V-I)]$ diagram in Fig. 6. Here we use our model grid to interpolate the results at a constant mass of 0.6 $M_\odot$ for both the DA and non-DA se-

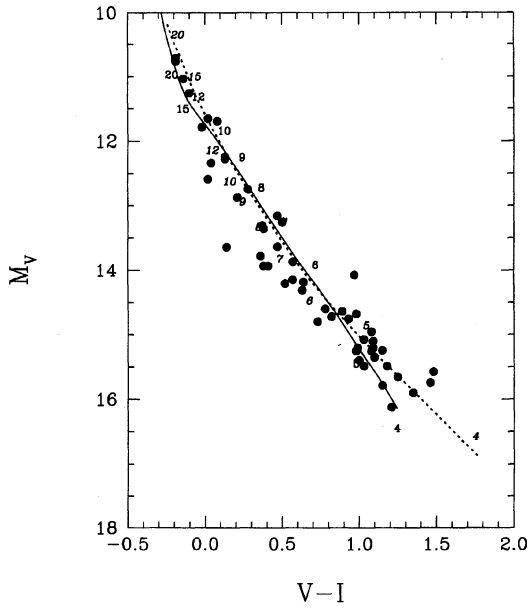

FIG. 6—[$M_V,(V-I)$] diagram for the 0.6 $M_\odot$ DA (solid line) and non-DA (dotted line) models. Temperatures are indicated in roman and italic fonts for the DA and non-DA models, respectively, in units of 10^3 K. The photometric and trigonometric parallax data is taken from Monet et al. (1992) and references therein.

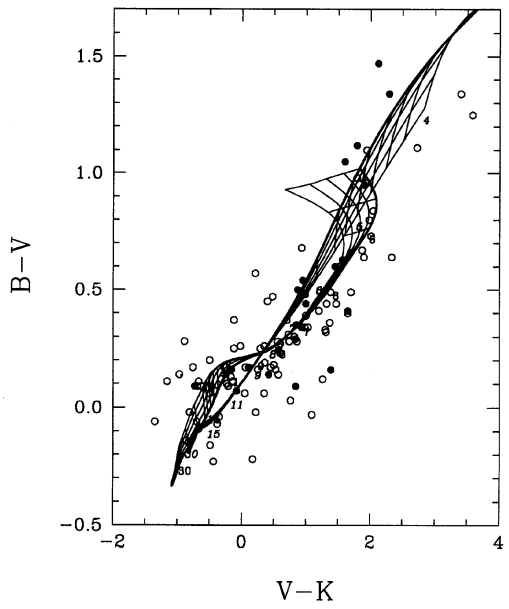

FIG. 7—[$(B-V)$,$(V-K)$] two-color diagram for the DA and non-DA model grids (the almost diagonal sequences represent the non-DA models). Temperatures are indicated as in Fig. 6; log g values are for 7.0 (0.5) 9.0 with the log g=7.0 models indicated by the thick solid lines. The observed photometry is taken from Probst (1983; open circles) and Leggett (1989; filled circles).

quences. This assumed mass reproduces well this sample, except perhaps in the $T_{\rm eff}$=6000−7000 K region where stars appear to be more massive regardless of their atmospheric composition. We make no distinction here between DA and non-DA stars.

Finally, we present the [$(B-V)$,$(V-K)$] diagram in Fig. 7. The data are taken from the infrared observations of Leggett (1989) who also provides a compilation of previously published infrared *JHK* photometry for cool white dwarfs. Additional infrared data from Probst (1983; mainly at *K*) are included as well. Even though the observational scatter is somewhat larger than in previous diagrams, the results of Fig. 7 indicate nevertheless that the observed photometry is well reproduced by our models. Again, we make no distinction between DA and non-DA stars since in cool white dwarfs, the absence of Hα does not necessarily imply a helium-rich composition. The more extensive spectroscopic and photometric survey of Ruiz et al. (1993) should help increase the sample of white dwarfs with infrared photometric data, and provide a better understanding of the chemical composition of these cool stars.

3.4 Strömgren Photometry

For the calculations of the Strömgren color indices, we use the transmission functions of Olson (1974) for u, b, and y, and that of Kodaira (1975) for v. The color calibration of Schulz (1978) was preferred to that of Olson (1974), since the latter is more appropriate for the calculations of color indices of main-sequence stars. Our results are reported in Tables 5 and 6 for the log g=8.0 pure hydrogen and pure helium models, respectively. Figure 8 displays the [$(u-b)$,$(b-y)$] diagrams for the DA and non-DA models, together with the observed photometry of Fontaine et al. (1985) for the DA stars, while that for the non-DA stars is taken from the catalog of spectroscopically identified white dwarfs of McCook and Sion (1987). No effort is made in the latter sample to select the best photometry. Instead we highlight in the non-DA panel the observations of Graham (1972) which should in principle be of higher quality. Indeed the

TABLE 5
Strömgren and Multichannel Color Indices for the Pure Hydrogen log g=8 Models

$T_{\rm eff}$(K)	$b-y$	$u-b$	$v-y$	$V-I$	$G-R$	$U-V$	$U-G$	$B-V$
4000	+0.736	+1.693	+1.466	+0.856	+1.137	+1.925	+1.427	+0.957
4500	+0.658	+1.502	+1.314	+0.725	+0.971	+1.681	+1.251	+0.831
5000	+0.578	+1.311	+1.158	+0.573	+0.795	+1.435	+1.075	+0.701
5500	+0.503	+1.138	+1.015	+0.429	+0.631	+1.210	+0.915	+0.581
6000	+0.428	+0.953	+0.871	+0.296	+0.472	+0.977	+0.748	+0.459
6500	+0.362	+0.795	+0.747	+0.180	+0.333	+0.777	+0.605	+0.351
7000	+0.310	+0.683	+0.655	+0.085	+0.221	+0.632	+0.506	+0.268
7500	+0.268	+0.613	+0.589	+0.004	+0.127	+0.535	+0.446	+0.204
8000	+0.231	+0.569	+0.543	−0.069	+0.044	+0.469	+0.412	+0.155
9000	+0.173	+0.557	+0.494	−0.202	−0.095	+0.421	+0.414	+0.089
10000	+0.130	+0.589	+0.481	−0.326	−0.212	+0.428	+0.454	+0.055
11000	+0.096	+0.605	+0.471	−0.429	−0.307	+0.424	+0.473	+0.032
12000	+0.066	+0.597	+0.455	−0.504	−0.380	+0.396	+0.465	+0.008
13000	+0.041	+0.580	+0.430	−0.551	−0.433	+0.359	+0.446	−0.018
14000	+0.015	+0.534	+0.385	−0.585	−0.481	+0.293	+0.403	−0.059
15000	−0.004	+0.470	+0.332	−0.608	−0.516	+0.214	+0.346	−0.102
16000	−0.020	+0.403	+0.285	−0.625	−0.543	+0.138	+0.285	−0.138
17000	−0.032	+0.337	+0.242	−0.640	−0.566	+0.064	+0.224	−0.168
20000	−0.059	+0.176	+0.150	−0.677	−0.615	−0.113	+0.073	−0.229
25000	−0.090	−0.022	+0.038	−0.724	−0.677	−0.330	−0.113	−0.303
30000	−0.112	−0.177	−0.055	−0.757	−0.719	−0.499	−0.260	−0.359
35000	−0.123	−0.275	−0.117	−0.771	−0.738	−0.604	−0.355	−0.392
40000	−0.130	−0.322	−0.150	−0.779	−0.750	−0.655	−0.400	−0.411
45000	−0.134	−0.351	−0.170	−0.785	−0.758	−0.687	−0.428	−0.423
50000	−0.138	−0.372	−0.185	−0.789	−0.764	−0.710	−0.447	−0.432
55000	−0.140	−0.387	−0.197	−0.792	−0.768	−0.727	−0.462	−0.438
60000	−0.143	−0.400	−0.206	−0.795	−0.772	−0.741	−0.474	−0.444
65000	−0.145	−0.410	−0.214	−0.798	−0.776	−0.753	−0.484	−0.449
70000	−0.146	−0.419	−0.221	−0.800	−0.779	−0.762	−0.493	−0.453
75000	−0.148	−0.427	−0.226	−0.802	−0.782	−0.771	−0.500	−0.457
80000	−0.149	−0.434	−0.232	−0.804	−0.784	−0.779	−0.507	−0.460
85000	−0.150	−0.440	−0.236	−0.806	−0.786	−0.785	−0.512	−0.463
90000	−0.151	−0.445	−0.240	−0.808	−0.788	−0.792	−0.517	−0.466
95000	−0.152	−0.450	−0.244	−0.809	−0.790	−0.797	−0.522	−0.468
100000	−0.153	−0.455	−0.248	−0.811	−0.792	−0.802	−0.526	−0.471

TABLE 6
Strömgren and Multichannel Color Indices for the Pure Helium log g=8 Models

$T_{\rm eff}$(K)	$b-y$	$u-b$	$v-y$	$V-I$	$G-R$	$U-V$	$U-G$	$B-V$
4000	+1.161	+2.850	+2.337	+1.435	+1.943	+3.370	+2.500	+1.677
4250	+1.035	+2.596	+2.101	+1.195	+1.663	+3.016	+2.258	+1.478
4500	+0.916	+2.344	+1.875	+0.987	+1.409	+2.673	+2.019	+1.288
4750	+0.807	+2.098	+1.664	+0.808	+1.185	+2.346	+1.787	+1.112
5000	+0.711	+1.863	+1.473	+0.658	+0.993	+2.042	+1.566	+0.953
5250	+0.628	+1.643	+1.304	+0.532	+0.829	+1.766	+1.362	+0.813
5500	+0.558	+1.445	+1.160	+0.427	+0.692	+1.524	+1.181	+0.695
6000	+0.453	+1.133	+0.942	+0.266	+0.486	+1.150	+0.898	+0.516
6500	+0.382	+0.921	+0.795	+0.152	+0.343	+0.898	+0.708	+0.396
7000	+0.330	+0.773	+0.689	+0.062	+0.235	+0.721	+0.576	+0.309
7500	+0.288	+0.658	+0.604	−0.014	+0.145	+0.579	+0.472	+0.239
8000	+0.251	+0.561	+0.531	−0.080	+0.067	+0.460	+0.384	+0.178
8500	+0.219	+0.477	+0.467	−0.137	−0.001	+0.356	+0.308	+0.126
9000	+0.191	+0.404	+0.411	−0.188	−0.060	+0.266	+0.243	+0.080
9500	+0.166	+0.340	+0.362	−0.232	−0.113	+0.187	+0.185	+0.039
10000	+0.144	+0.284	+0.318	−0.272	−0.159	+0.117	+0.134	+0.003
11000	+0.110	+0.194	+0.250	−0.337	−0.236	+0.006	+0.053	−0.054
12000	+0.081	+0.121	+0.195	−0.392	−0.300	−0.084	−0.012	−0.103
13000	+0.059	+0.065	+0.154	−0.438	−0.354	−0.152	−0.061	−0.143
14000	+0.041	+0.024	+0.124	−0.478	−0.399	−0.202	−0.095	−0.178
15000	+0.028	−0.003	+0.104	−0.514	−0.439	−0.235	−0.116	−0.208
17000	+0.012	−0.028	+0.089	−0.576	−0.502	−0.264	−0.131	−0.252
18000	+0.007	−0.034	+0.087	−0.602	−0.528	−0.270	−0.133	−0.268
20000	−0.001	−0.050	+0.078	−0.644	−0.570	−0.287	−0.141	−0.294
22000	−0.011	−0.068	+0.063	−0.671	−0.599	−0.309	−0.155	−0.314
24000	−0.018	−0.077	+0.053	−0.682	−0.612	−0.322	−0.162	−0.325
26000	−0.028	−0.091	+0.037	−0.693	−0.628	−0.343	−0.175	−0.340
28000	−0.042	−0.115	+0.013	−0.710	−0.650	−0.377	−0.197	−0.361
30000	−0.055	−0.145	−0.014	−0.723	−0.669	−0.417	−0.225	−0.378

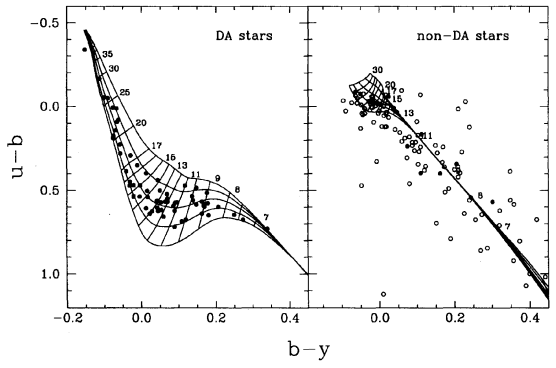

FIG. 8—[$(u-b),(b-y)$] Strömgren two-color diagrams for the DA and non-DA models with $T_{\rm eff}$ indicated in units of 10^3 K, and log g values of 7.0 (0.5) 9.0 (from bottom to top). The observed photometry for the DA stars is taken from Fontaine et al. (1985) and that for the non-DA stars is from McCook and Sion (1987; open circles) and Graham (1972; filled circles).

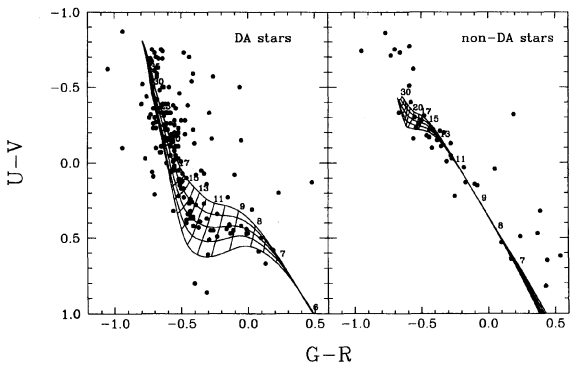

FIG. 9—[$(U-V),(G-R)$] multichannel two-color diagrams for the DA and non-DA models with $T_{\rm eff}$ indicated in units of 10^3 K, and log g values of 7.0 (0.5) 9.0 (from bottom to top). The observed photometry is taken from Green et al. (1986).

observed scatter with Graham's data alone is significantly reduced. The Strömgren photometry reproduces the trends observed in previous two-color diagrams. Note, however, the small discrepancy with the hottest non-DA stars whose mean surface gravity appears lower than average. This discrepancy could be the result of an inadequate color transformation, as discussed by Koester et al. (1981).

3.5 Multichannel Photometry

The multichannel photometric system and its application to white-dwarf stars are discussed, for instance, by Greenstein (1976). The magnitudes are represented by values of m_ν measured at $1/\lambda$ (μm^{-1}), and designated $U(m_{2.80})$, $B(m_{2.35})$, $G(m_{2.12})$, $V(m_{1.85})$, $R(m_{1.44})$, and $I(m_{1.25})$. The individual bandpasses can be approximated by boxes whose resolution depends on the setup used with the multichannel spectrograph. In the following, we simply adopt 80 Å for U, B, G, and V, and 160 Å for the remaining filters. Given the large number of possible color indices, we restrict our calculations to those used by Greenstein (1984), i.e., $V-I$, $G-R$, $U-V$, $U-G$, and $B-V$. These color indices are reported in Tables 5 and 6 for the log $g=8.0$ model atmospheres with pure hydrogen and pure helium compositions, respectively.

The [$(U-V),(G-R)$] two-color diagrams for the DA and non-DA models are presented in Fig. 9, together with the observed multichannel photometry of Green et al. (1986). Since this data set is taken from a blue-excess colorimetric survey, the white dwarfs displayed in Fig. 9 are hotter, on average, than the stars shown in previous diagrams. In particular, the non-DA stars include several hot DO white dwarfs. As before, there is a general good agreement with the observed location of the DA stars, although the observational scatter remains important. The region covered by the hottest DB stars is also well reproduced.

3.6 Average V Flux

Analyses of energy distributions often require a flux normalization at V. Even though, in many cases, it is probably a sufficient approximation for white-dwarf spectra to use the monochromatic flux interpolated at a given effective wavelength, a more accurate value of the average flux at V is given by

$$H_V=\frac{\int_0^\infty H_\lambda S_V(\lambda)d\lambda}{\int_0^\infty S_V(\lambda)d\lambda}. \quad (9)$$

These average V fluxes are reported in Tables 1 and 2. The effective wavelength is $\lambda_{\rm eff}=5510$ Å, and is defined as

$$\lambda_{\rm eff}=\frac{\int_0^\infty \lambda S_V(\lambda)d\lambda}{\int_0^\infty S_V(\lambda)d\lambda}. \quad (10)$$

4. CONCLUDING REMARKS

We have presented a summary of a complete set of color-index and magnitude calculations for DA and non-DA stars. Other quantities of interest such as stellar masses and ages have been provided as well, and can be used to calculate sequences at a constant *mass* value instead of a constant log g value. We have also illustrated the validity and relevance of our calculations to the study of nearby white dwarfs. These results can be used, to some extent, as a template against which independent studies of open or globular clusters can be compared. Our complete set of calculations can be made available upon request by contacting the first author (electronic mail: bergeron@astro.umontreal.ca). With these tools in hand, these calculations can readily be extended to any given filter system, such as the *HST* photometric system for instance.

We are grateful to Conard Dahn for giving us access to the USNO photometric and trigonometric parallax data, and to M. A. Wood for providing us with unpublished evolutionary models. This work was supported in part by the NSERC Canada, and by the Fund FCAR (Québec).

REFERENCES

Allen, C. W. 1973, Astrophysical Quantities (London, Athlone)
Beauchamp, A. 1995, Ph.D. thesis, Univ. de Montréal

Beauchamp, A., Wesemael, F., Bergeron, P., and Liebert, J. 1995, ApJ, 441, L85
Bergeron, P., Saffer, R. A, and Liebert, J. 1992, ApJ, 394, 228
Bergeron, P., Saumon, D., and Wesemael, F. 1995a, ApJ, 443, 764
Bergeron, P., Wesemael, F., and Fontaine, G. 1991, ApJ, 367, 253
Bergeron, P., Wesemael, F., Lamontagne, R., Fontaine, G., Saffer, R. A., and Allard, N. F. 1995b, ApJ, 449, 258
Bessel, M. S. 1990, PASP, 102, 1181
Bessel, M. S., and Brett, J. M. 1988, PASP, 100, 1134
Castelli, F., and Kurucz, R. L. 1994, A&A, 281, 817
De Marchi, G., and Paresce, F. 1995, A&A, in press
Elson, R. A. W., Gilmore, G. F., Santiago, B. X., and Casertano, S. 1995, AJ, in press
Fontaine, G., Bergeron, P., Lacombe, P., Lamontagne, R., and Talon, A. 1985, AJ, 90, 1094
Fusi Pecci, F., and Renzini, A. 1979, in Astronomical Uses of the Space Telescope, ed. F. Macchetto et al. (Geneva, ESO), p. 181
Graham, J. A. 1972, AJ, 77, 144
Green, R. F., Schmidt, M., and Liebert, J. 1986, ApJS, 61, 305
Greenstein, J. L. 1976, AJ, 81, 323
Greenstein, J. L. 1984, ApJ, 276, 602
Hamada, T., and Salpeter, E. E. 1961, ApJ, 134, 683
Hayes, D. S. 1985, in IAU Symp. 111, Calibration of Fundamental Stellar Quantities, ed. D. S. Hayes, L. E. Pasinetti, and A. G. Davis Philip (Dordrecht, Reidel), p. 225
Hummer, D. G., and Mihalas, D. 1988, ApJ, 331, 794
Kodaira, K. 1975, in Problems in Stellar Atmospheres and Envelopes, ed. B. Baschek, W. H. Kegel, and G. Traving (Berlin, Springer), p. 149
Koester, D., Schulz, H., and Wegner, G. 1981, A&A, 102, 331
Koester, D., Schulz, H., and Weidemann, V. 1979, A&A, 76, 262
Leggett, S. K. 1989, A&A, 208, 141
Leggett, S. K. 1992, ApJS, 82, 351
Matthews, T. A., and Sandage, A. R. 1963, ApJ, 138, 30
McCook, G. P., and Sion, E. M. 1987, ApJS, 65, 603
Monet, D. G., Dahn, C. C., Vrba, F. J., Harris, H. C., Pier, J. R., Luginbuhl, C. B., and Ables, H. D. 1992, AJ, 103, 638
Mountain, C. M., Leggett, S. K. Selby, M. J., Blackwell, D. E., and Petford, A. D. 1985, A&A, 151, 399
Oke, J. B., Weidemann, V., and Koester, D. 1984, ApJ, 281, 276
Olson, E. C. 1974, PASP, 86, 80
Paresce, F., De Marchi, G., and Romaniello, M. 1995, ApJ, 440, 216
Probst, R. G. 1983, ApJS, 53, 335
Richer, H. B. et al. 1995, ApJ, in press
Ruiz, M. T., Bergeron, P., and Leggett, S. K. 1993, in White Dwarfs: Advances in Observation and Theory, ed. M. A. Barstow (NATO ASI Series) (Dordrecht, Kluwer), p. 245
Schulz, H. 1978, A&A, 68, 75
Shipman, H. L., and Sass, C. A. 1980, ApJ, 235, 177
Stancil, P. C. 1994, ApJ, 430, 360
van Altena, W. F., Lee, J. T., and Hoffleit, E. D. 1994, The General Catalogue of Trigonometric Parallaxes (New Haven, Yale University Observatory)
von Hippel, T., Gilmore, G., and Jones, D. H. P. 1995, MNRAS, 273, L39
Weidemann, V., and Koester, D. 1984, A&A, 132, 195
Wesemael, F., Auer, L. H., Van Horn, H. M., and Savedoff, M. P. 1980, ApJS, 43, 159
Winget, D. E., Hansen, C. J., Liebert, J., Van Horn, H. M., Fontaine, G., Nather, R. E., Kepler, S. O., and Lamb, D. Q. 1987, ApJ, 315, L77
Wood, M. A. 1990, Ph.D. thesis, Univ. of Texas at Austin
Wood, M. A. 1992, ApJ, 386, 539
Wood, M. A. 1995, in 9th European Workshop on White Dwarfs, NATO ASI Series, ed. D. Koester and K. Werner (Berlin, Springer) (in press)